

Validation and extrapolation of atomic mass with physics-informed fully connected neural network

Yiming Huang ^{1,2,3} Jinhui Chen ^{1,2,*} Jiangyong Jia ^{4,5,†}
Lu-Meng Liu ^{6,‡} Yu-Gang Ma ^{1,2,§} and Chunjian Zhang ^{1,2,4,¶}

¹*Key Laboratory of Nuclear Physics and Ion-beam Application (MOE),
and Institute of Modern Physics, Fudan University, Shanghai 200433, China*

²*Shanghai Research Center for Theoretical Nuclear Physics, NSFC and Fudan University, Shanghai 200438, China*

³*College of Physics, Jilin University, Changchun 130012, China*

⁴*Department of Chemistry, Stony Brook University, Stony Brook, NY 11794, USA*

⁵*Physics Department, Brookhaven National Laboratory, Upton, NY 11976, USA*

⁶*Physics Department and Center for Particle Physics and Field Theory, Fudan University, Shanghai 200438, China*

Machine learning offers a powerful framework for validating and predicting atomic mass. We compare three improved neural network methods for representation and extrapolation for atomic mass prediction. The powerful method, adopting a macroscopic-microscopic approach and treating complex nuclear effects as output labels, achieves superior accuracy in AME2020, yielding a much lower root-mean-square deviation of 0.122 MeV in the test set, significantly lower than alternative methods. It also exhibits a better extrapolation performance when predicting AME2020 from AME2016, with a root-mean-square deviation of 0.191 MeV. We further conduct sensitivity analyses against the model inputs to verify interpretable alignment beyond statistical metrics. Incorporating theoretical predictions of magic numbers and masses, our fully connected neural networks reproduce key nuclear phenomena including nucleon pairing correlation and magic number effects. The extrapolation capability of the framework is discussed and the accuracy of predicting new mass measurements for isotope chains has also been tested.

I. INTRODUCTION

The atomic nucleus, composed of nucleons (protons and neutrons), represents a complex quantum many-body system [1, 2]. Its mass is a fundamental property critical for understanding the strong nuclear forces [3], equation of state of the neutron stars [4, 5], nuclear structure [6], stellar evolution and r -process nucleosynthesis processes [2, 7–9]. However, the persistent pursuit of a precise nuclear mass remains an urgent challenge, which is benefitted from the advancements in nuclear facilities. Measurements on the neutron-rich side of the nuclear chart remain inaccessible, leaving most r -process nuclei unexplored [10]. The neutron drip line has been experimentally confirmed only for nuclei with proton numbers up to $Z=10$. The exact boundaries of the nuclear landscape remain experimentally unknown. Consequently, our understanding of atomic properties far from stability and the ultimate limits of the nuclear landscape relies primarily on theoretical calculations [11].

Atomic Mass Evaluation (AME) provides reliable and comprehensive experimental measurements of atomic masses [12–17]. Theoretically, numerous models developed to pursue nuclear mass properties, have also achieved significant progress. One of the earliest approaches involved constructing phenomenological empir-

ical models, the Bethe-Weizsäcker (BW) formula, which treats the nucleus as a charged liquid drop and approximates nuclear masses with 3 MeV accuracy [18–20]. More accurate nuclear mass descriptions have been achieved using macroscopic-microscopic models, including the Finite Range Droplet model (FRDM2012) [21], Hartree-Fock-Bogoliubov (HFB) model [22, 23], and Weizsäcker-Skyrme (WS4) [24]. Covariant density functional theory (CDFT) provides a robust framework for studying nuclear structure successfully [25–27]. Within this framework, the relativistic continuum Hartree-Bogoliubov (RCHB) method [28], employing the relativistic density functional PC-PK1 [29] has been significantly successful in studying both stable and exotic nuclei. The deformed relativistic Hartree-Bogoliubov theory in the continuum (DRHBc) has been applied to even-even nuclei [30] and even- Z nuclei [31], yielding root-mean-square deviation (RMSD) of 1.518 MeV and 1.433 MeV, respectively. Notably, WS4 delivers the highest accuracy, with an RMSD of 0.298 MeV [24]. However, model accuracy deteriorates notably for heavier nuclei, especially those far from the β -stability line, with errors sometimes reaching several MeV [32]. This uncertainty presents a significant challenge for reliable predictions of exotic nuclear properties [33].

In recent years, artificial intelligence (AI) has emerged as a transformative tool in nuclear physics, with machine learning (ML) algorithms significantly enhancing predictive accuracy and extrapolation capabilities. ML has been increasingly applied to various aspects of nuclear physics, achieving notable successes in predicting atomic masses [20, 32, 34–37], nucleon density distributions, charge radii [38, 39], charge density distributions,

* chenjinhui@fudan.edu.cn

† jiangyong.jia@stonybrook.edu

‡ liulumeng@fudan.edu.cn

§ mayugang@fudan.edu.cn

¶ chunjianzhang@fudan.edu.cn

β decay rates [40], α decay rates [36, 41, 42], reaction cross-sections [43, 44], quadrupole deformations [45, 46], and heavy-ion collision [47–57]. Especially, ML has been widely applied in prediction of nuclear mass, including Artificial Neural Networks (ANNs) [35–37, 58], Bayesian Neural Networks (BNNs) [20, 39], Convolutional Neural Networks (CNNs)[34], Light Gradient Boosting Machine (lightGBM) [59], Support Vector Machines (SVMs) [60], and Bayesian Gaussian Processes (BGP) [61].

Fully Connected Neural Networks (FCNNs) provide a simple yet effective framework for capturing nonlinear relationships, making them well suited for small-scale regression problems [62, 63]. FCNNs can also effectively model the complex, nonlinear interactions between nuclear structure variables, such as proton/neutron number and binding energies. Moreover, FCNNs are particularly suitable for nuclear physics tasks, where atomic mass data is often limited. Compared to more complex architectures, FCNNs are computationally efficient and less prone to overfitting, which makes them an ideal choice for this specific task. In this study, we used FCNNs to predict nuclear masses, with the framework enhanced through the integration of two complementary strategies: direct nuclear mass prediction and residual correction between theoretical and experimental values. In addition, effective auxiliary outputs are introduced to accelerate training convergence and improve predictive accuracy by focusing on challenging-to-represent components; thereby, they enhance both training efficiency and representation quality.

Our findings show that the prediction of residual components is more effective than direct mass predictions, allowing the FCNN to address theoretical limitations with improved accuracy and interpretability. Sensitivity analysis and physical evaluations further confirm that the model captures key nuclear phenomena, such as shell corrections and pairing effects, validating its physics-driven utility. The integration of auxiliary outputs and physics-informed features highlight a strong synergy between machine learning and nuclear theory, significantly improving performance, robustness, and interpretability for precise nuclear property predictions.

The paper is organized as follows. The details of the methodology and FCNN framework are discussed in Sect. II. Section III provides the results and discusses the validation and extrapolation abilities of the proposed models. The summary and outlook are given in Sect. IV.

II. METHODOLOGY AND FRAMEWORK

A. Mass data

To capture the statistical properties of nucleons, we analyze the binding energy E for the nuclei with proton and neutron numbers exceeding 20, yielding 2162 and 2087 records from AME2020 [64] and AME2016 [65], respectively. These datasets are divided into training and

test sets for neural networks. Fig. 1 illustrates the distribution of the nuclei used for training and testing, highlighting the characteristics of the dataset utilized in subsequent model development.

Distinct preprocessing strategies are applied to input features and output labels. Input features are scaled to $[0, 1]$ using *MinMaxScaler* from *PyTorch*, maintaining consistency even for binary variables. Output labels are normalized to accelerate training and ensure outputs have a similar scale, improving gradient stability and prediction accuracy. Preprocessing parameters for both input features and output labels are derived solely from the training set to avoid data leakage. Predicted outputs are subsequently unscaled to recover the original nuclear binding energy.

B. Model evaluations

The prediction accuracy and extrapolation capacity were quantified using the RMSD and mean absolute deviation (MAE), defined as:

$$\begin{aligned} \text{RMSD} &= \sqrt{\frac{1}{N} \sum_{i=1}^N (E^{\text{nn}} - E^{\text{exp}})^2}, \\ \text{MAE} &= \frac{1}{N} \sum_{i=1}^N |E^{\text{nn}} - E^{\text{exp}}|, \end{aligned} \quad (1)$$

where E^{nn} represents neural network prediction and E^{exp} denotes the experimental value.

Statistical analysis of a network’s predictions is insufficient to confirm its adherence to physical principles. Evaluating whether input influences align with physical laws is essential. Sensitivity analysis quantifies the impact of each input feature on prediction quality. The normalized gradient method is employed to access the contributions of input features. This approach computes the absolute gradient of the neural network with respect to each feature and normalizes the values to determine relative importance. Gradients are derived from all available data during training and evaluation. The sensitivity score and normalized sensitivity score are defined as:

$$\begin{aligned} S_j &= \frac{1}{N} \sum_{i=1}^N \left| \frac{\partial y_i}{\partial x_j} \right|, \\ S_j^{\text{norm}} &= \frac{S_j}{\sum_{j=1}^M S_j}, \end{aligned} \quad (2)$$

where S_j denotes the sensitivity score of the j -th feature, N is the number of samples, y_i is the model output for the i -th sample, and x_j is the j -th input feature. S_j^{norm} represents normalized sensitivity score, with M being the total number of features.

The models selected for subsequent experiments are evaluated according to three key criteria. The model must perform well on the training and test sets, with

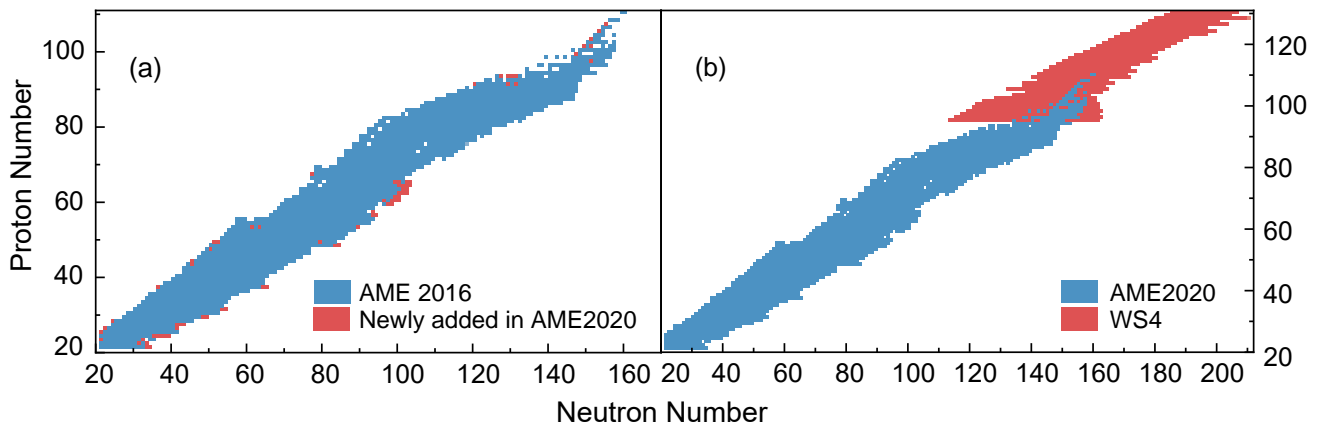


FIG. 1. (a) The mass data were selected from the AME2020 and AME2016 datasets, with $Z, N > 20$, and only the nuclei with experimental errors less than 100 keV were used. (b) The mass data were selected from the AME2020 dataset for nuclei with $Z, N > 20$, and only the nuclei with experimental errors less than 100 keV were used. For superheavy elements ($Z > 94$), predictions were supplemented using the WS4 model.

closely aligned results, ensuring good generalization. Input features must align with the underlying physical background to evaluate their impact on the output. For the extrapolation task concerning the superheavy nuclei far from the β -stability line, the results must not only satisfy numerical accuracy from the first criterion but also reflect physical phenomena driven by input features in the training set, capturing embedded physical information.

C. Input features and theoretical framework

We extract the input features using a macroscopic-microscopic approach that combines two models: the improved semi-classical liquid drop model and the shell model. This approach incorporates the physical background into the input features.

The improved semi-classical liquid drop model describes the nucleus as a positively charged, incompressible droplet with nucleons behaving like molecules. The binding energy in the improved liquid drop model can be expressed as [66]

$$E_{\text{LD}}(A, Z) = E_v + E_s + E_C + E_{\text{sym}} + E_{\text{pair}}, \quad (3)$$

where the right-hand side represents the following terms:

$$\begin{aligned} E_v &= a_v A, \\ E_s &= a_s A^{2/3}, \\ E_C &= a_c \frac{Z^2}{A^{1/3}} \left(1 - Z^{-2/3}\right), \\ E_{\text{sym}} &= a_{\text{sym}} I^2 A, \\ E_{\text{pair}} &= a_{\text{pair}} A^{-1/3} \delta_{np}. \end{aligned} \quad (4)$$

These terms correspond to volume energy, surface energy, Coulomb energy, asymmetry energy, and pairing energy,

respectively. Here, a_i are the corresponding coefficients, $I = (N - Z)/A$ is the isospin asymmetry, and δ_{np} encodes the parity of the nucleus (whether it is odd or even in neutron and proton numbers).

The shell model provides a fundamental framework for understanding nuclear stability, particularly near magic numbers [67]. To quantify this, the valence proton number V_p and valence neutron number V_n are introduced as input features. These are defined as

$$\begin{aligned} V_p &= Z - Z_{\text{core}}, \\ V_n &= N - N_{\text{core}}, \end{aligned} \quad (5)$$

where Z_{core} and N_{core} denote the nearest magic numbers smaller than the given Z and N . In this study, the magic number adopted is ($Z = 20, 28, 50, 82, 114, 120$ and $N = 20, 28, 50, 82, 126, 184, 198$), based on the reference [68–70].

The general input features derived from the above descriptions are listed in Tab. I and expressed as follows. Z and A characterize the nuclear species, with the binding energy depending on both. A represents the volume energy, while $A^{2/3}$ reflects the surface energy, and E_C/a_c represents the Coulomb energy. The symmetry energy is described by $I^2 A$ and $|I|$. Finally, $A^{-1/3}$ and δ_{np} reflect the contribution of the pairing term. Additionally, for the shell correction, we introduce V_p and V_n , representing the valence protons and neutrons, respectively.

In addition to the aforementioned general input features, we explore three distinct methods to incorporate the effects of deformation, microscopic corrections, and multi-output, as outlined in Tab. I.

1. Method I

In this method, we consider versions of the liquid droplet model where the pairing term takes the form

TABLE I. Input and output features in Method I, II, and III.

Methods	Input Features	Output Features
I	$Z, A, A^{2/3}, E_C/a_c, I^2 A, I , A^{-1/3}, V_p, V_n, \delta_{np}, A^{-1/2}$	E^{exp}
II	$Z, A, A^{2/3}, E_C/a_c, I^2 A, I , A^{-1/3}, V_p, V_n, \delta_{np}, g_1 A^{1/3}, g_2 A^{-1/3}$	$E_{\text{LD}}, E^{\text{exp}}, E^{\text{exp}} - E_{\text{LD}}$
III	$Z, A, A^{2/3}, E_C/a_c, I^2 A, I , A^{-1/3}, V_p, V_n, \delta_{np}, \prod_{k \geq 2} b_k \beta_k^2$	$E_{\text{LD}}, E^{\text{exp}}, E^{\text{exp}} - E_{\text{LD}}$

$E_{\text{pair}} = a_{\text{pair}} A^{-1/2} \delta_{np}$ [71]. To incorporate this, we introduce an additional input feature $A^{-1/2}$ to compete with the $A^{-1/3}$ term discussed above. We encode δ_{np} as a two-dimension vector using the following definition:

$$\delta_{np} = \begin{cases} (1, 0), & \text{if } N \text{ and } Z \text{ are even} \\ (0, 1), & \text{if } N \text{ and } Z \text{ are odd} \\ (0, 0), & \text{other.} \end{cases} \quad (6)$$

For the output features, we adopt the experimental binding energy E^{exp} exclusively.

2. Method II

To enhance prediction accuracy, we developed an alternative approach, Method II, which incorporates revised input features, output features, and network architecture for comparison with Method I. The total binding energy of a nucleus, which includes deformation and Strutinsky shell corrections, $E'(A, Z, \beta)$, is expressed as

$$E(A, Z, \beta) = E_{\text{LD}}(A, Z) \prod_{k \geq 2} (1 + b_k \beta_k^2) + E'(A, Z, \beta), \quad (7)$$

where the curvature of the parabola for a given β_k ($k = 2, 4, 6$) deformation is approximately described by the empirical formula [66]

$$b_k = \left(\frac{k}{2}\right) g_1 A^{1/3} + \left(\frac{k}{2}\right)^2 g_2 A^{-1/3}. \quad (8)$$

Given the limited data available for β_k and its dependence on A and Z , its effects are captured indirectly through these variables. Moreover, the contribution of b_k is modeled by decomposing it into two components for the network input: $g_1 A^{1/3}$ and $g_2 A^{-1/3}$. The macro-micro model, as described in Eq. (7), extends the liquid-drop model by incorporating both deformation and microscopic corrections. Neural networks typically perform better when the output labels are strongly correlated [72, 73].

In this method, we introduce two additional output labels to constrain the primary target, the difference between experimental values and those of the liquid-drop model. This constraint enhances the loss function and improves the accuracy of prediction. Theoretical binding energies, which are highly accurate, are excluded as output labels to avoid redundancy. However, predicting

experimental values introduce a challenge, as it risks conflating microscopic and macroscopic corrections, which will potentially increase the error. To address this issue, we isolate the microscopic component by subtracting the macroscopic part (including the droplet and deformation terms) from the total binding energy. This approach allows the model to focus specifically on capturing the intricate microscopic features.

To better leverage experimental and theoretical data, we propose a multi-output approach with three output labels: the experimental binding energy (E^{exp}), the liquid-drop model binding energy (E_{LD}), and their difference ($E^{\text{exp}} - E_{\text{LD}}$), as listed in Tab. I (Method II). This strategy results in significantly improved accuracy over Method I. The parameters used to calculate E_{LD} in this method are taken from Ref. [66].

3. Method III

In this method, we adopt a strategy similar to Method II but with a few minor adjustments, as listed in Tab. I (Method III). Specifically, the Coulomb term differs from that in Eq. (4) and takes the following form, as used in the WS4 model [24].

$$E_C = a_c \frac{Z^2}{A^{1/3}} \left(1 - 0.76 Z^{-2/3}\right). \quad (9)$$

Next, the parameter δ_{np} is encoded as follows

$$\delta_{np} = \begin{cases} 2 - |I|, & \text{if } N \text{ and } Z \text{ are both even} \\ |I|, & \text{if } N \text{ and } Z \text{ are both odd} \\ 1 - |I|, & \text{if } N \text{ is even, } Z \text{ is odd, and } N > Z \\ 1 - |I|, & \text{if } N \text{ is odd, } Z \text{ is even, and } N < Z \\ 1, & \text{if } N \text{ is even, } Z \text{ is odd, and } N < Z \\ 1, & \text{if } N \text{ is odd, } Z \text{ is even, and } N > Z. \end{cases} \quad (10)$$

For the deformation contribution, we replace the terms $g_1 A^{1/3}$ and $g_2 A^{-1/3}$ in Eqs. (7) and (8) with the summation form defined as $def = \prod_{k \geq 2} b_k \beta_k^2$, which provides a more accurate description of the nuclear shape. Finally, the parameters used to calculate E_{LD} in this method and β_k for the given nucleus are taken from Ref. [24]. Through these adjustments, this method achieves improved accuracy while maintaining a framework similar to that of Method II.

D. Network architecture

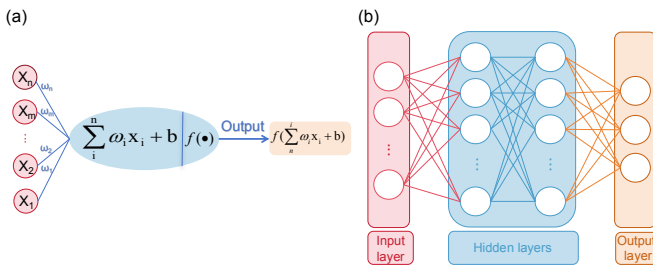


FIG. 2. (a) The single-layer perceptron consists of an input layer, weights, a bias, and an output layer, performing a nonlinear mapping via a linear transformation and activation function f . (b) The FCNN is composed of multiple SLPs, with numerous weights and bias terms.

An FCNN with two hidden layers was used for optimal feature representation and prediction. The first layer, 80–120 neurons, captured input features, while the second, with 40–60 neurons, refined these features. This design balances model complexity and efficiency, ensuring adaptability to diverse samples. Preliminary experiments revealed that the slightly prediction of binding energy was improved by adding 1-5 layers but the training time and overfitting risks were also increased. Similarly, increasing neurons per layer up to 500 enhanced the performance but posed similar challenges. In contrast, the overly simple network led to slower training and poor fitting. These findings highlight the need to balance network complexity and generalization for efficient training and robust performance. The mechanisms of the single-layer perceptron (SLP) and the neural network architecture are illustrated in Fig. 2.

We selected the GELU activation function in FCNN for its smooth transition between positive and negative values, enhancing gradient flow and enabling neurons to fully learn input features with physical significance. GELU outperforms ReLU and Leaky-ReLU in mitigating gradient vanishing issues and is more accurate and efficient for regression problems than Sigmoid and Tanh [74, 75].

We avoided decay mechanisms like Adam’s learning rate (LR) decay or cosine decay, which can cause the optimizer to get stuck in local minima. Instead, we manually adjusted the learning rate based on loss behavior. Initially, a larger learning rate was used, and when the loss oscillated near local minima, we reduced the learning rate for subsequent training. This approach enhanced adaptability to the problem’s specific conditions.

The Huber loss function is used for its robustness to outliers. Unlike squared loss, it remains stable with large discrepancies between theoretical and experimental values, preventing overfitting. Its differentiability when values match makes it effective for regression tasks, defined

as follows

$$L_{\text{Huber}} = \begin{cases} \frac{1}{2}(E^{\text{nn}} - E^{\text{exp}})^2, & |E^{\text{nn}} - E^{\text{exp}}| \leq \delta, \\ \delta \cdot (|E^{\text{nn}} - E^{\text{exp}}| - \frac{1}{2}\delta), & |E^{\text{nn}} - E^{\text{exp}}| > \delta, \end{cases} \quad (11)$$

with $\delta = 1$, E^{nn} is FCNN’s prediction as a function of model weights and bias, and E^{exp} is the experimental value.

To improve the network’s generalization and ensure consistent performance across training and test sets, we introduce L_2 regularization. This technique adds the sum of squared model parameters (L^2 norm) as a penalty term to the loss function, keeping model weights small. For our regression task, L_2 regularization is applied via weight decay in the Adam optimizer. The modified loss function is

$$L_{\text{reg}}(w) = L(w) + \frac{\lambda}{2} \|w\|_2^2, \quad (12)$$

with λ controls the regularization strength.

III. RESULTS AND DISCUSSIONS

We study three different cases across three FCNN methods. In Case A, models were trained on AME2020 mass data and split 8:2 into training and test sets. All the methods demonstrated strong performance, accurately representing nuclear masses. To further examine the models, a sensitivity analysis was conducted to assess the impact of input features on outputs, providing insights into the neural networks and making the “black box” appear slightly more transparent. In Case B, we assessed the models’ extrapolation abilities by training on AME2016 data and predicting newly added data in AME2020. Through optimization, the neural networks achieved reasonable extrapolation capability. In Case C, building on the superior performance, extrapolation capability, and efficiency of the second method, we expanded Case A’s dataset to include WS4 model results, which were absent in the AME2020 data. Following the same training and validation protocol, we verified the predicted outputs by calculating physical quantities to ensure consistency with governing physical laws.

A. Case A: performance in the AME2020

Figure 3 shows the sensitivity analysis in three distinct methods in Case A. As observed, macroscopic features dominate in Method I, while microscopic features derived from the shell model exert a stronger influence in Method II and III. Variations in δ_{np} show less impact on all the results, as Method I focuses on the overall binding energy predictions, and Method II targets the more challenging region-dominated nuclear shell effects. Although δ_{np} are highly correlated with A and Z , and thus partially embedded in other features, their significance

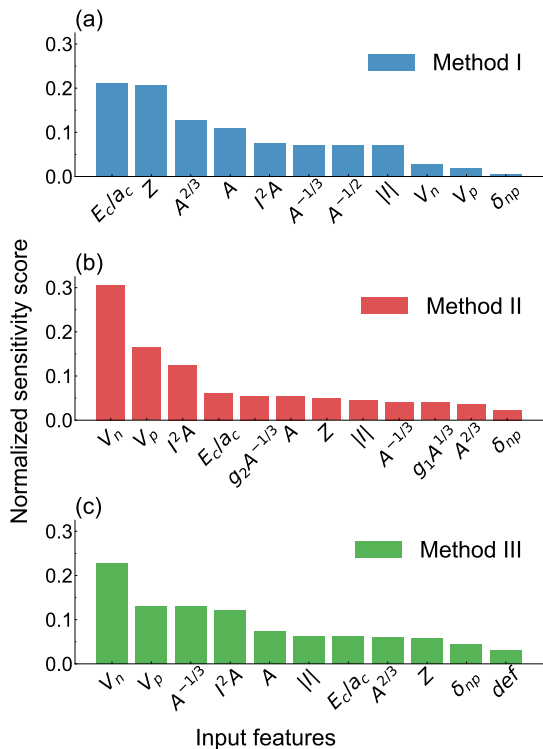


FIG. 3. Comparison of normalized sensitivity analysis in different input features among three Methods.

remains indispensable. To validate this, we conducted ablation tests using the same optimization strategies as before. For Method I, the training and test RMSD are 0.756 MeV and 0.852 MeV, respectively, while Method II’s training and test RMSD are 0.181 MeV and 0.223 MeV, respectively. Method III’s training and test RMSD are 0.172 MeV and 0.196 MeV. In Method III, variations in def show less impact on predictions, and we also conducted an ablation test by removing def while using the same optimization strategies as before. Finally, Method III’s training and test RMSD are 0.069 MeV and 0.154 MeV, respectively. These results indicate that Method I relies more on δ_{np} but all the methods require them as inputs to achieve optimal performance.

In Case A, we select the mass data from AME2020 with absolute errors less than 100 keV and $Z, N > 20$. To ensure reproducibility and minimize the impact of data splitting, we applied a specific data shuffling strategy with $random_state = 42$, a parameter for pseudo-random number generation in *Scikit-learn*. All the methods used the same neural network architecture, consisting of two hidden layers with 80 and 40 neurons, respectively, to compare their extrapolation capabilities. In Method I, we observed that achieving strong performance on both the training and test sets required a significantly prolonged training process, with a risk of local minima. To address this, a dynamic learning rate was employed, adjusting according to the loss function value, as shown in Tab. II Case A. Meanwhile, an L_2 regularization coefficient

TABLE II. Loss function vs. learning rate for Case A, B, and C in three Methods.

Case	Method	Loss function ($\times 10^{-6}$)	Learning rate ($\times 10^{-6}$)
A	I	≥ 40 [10, 40) [7.5, 10) [6, 7.5) < 6	3000 500 50 20 3
	II/III	≥ 0	1000
B	I	≥ 50 [25, 50) [20, 25) [12, 20) [10, 12) [8, 10) < 8	3000 1000 500 100 20 10 3
	II/III	≥ 0	100
C	III	≥ 50 [20, 50) < 20	3000 500 100

TABLE III. Training and test set errors for Case A, B, and C in three Methods.

Case	Method	Datasets	RMSD (MeV)	MAE (MeV)
A	I	Training	0.135	0.099
		Test	0.204	0.141
		All	0.151	0.107
	II	Training	0.087	0.064
		Test	0.143	0.099
		All	0.101	0.071
	III	Training	0.052	0.039
		Test	0.122	0.087
		All	0.071	0.049
B	I	Training	0.195	0.145
		Test	0.416	0.283
		All	0.207	0.150
	II	Training	0.159	0.122
		Test	0.237	0.173
		All	0.162	0.124
	II	Training	0.125	0.096
		Test	0.191	0.144
		All	0.128	0.097
C	III	Training	0.116	0.082
		Test	0.161	0.107
		All	0.126	0.087

of 5×10^{-8} was applied. Unlike Method II, this approach did not require pre-experimentation for early stopping. Training was halted after 2.5 million epochs, when performance stabilized within 2–3 million epochs. The resulting RMSD for the training set was 0.135 MeV, with an MAE of 0.099 MeV, as shown in Tab. III Case A. For the test set, their values were 0.204 and 0.141 MeV, indicating strong generalization. We also list the resulting values calculated from all datasets.

Method II and III adopt the same network structure selected by preliminary experiments, training, and division of test set as Method I. An early stopping strategy,

shown in Fig. 4 (a) and (c) for Method II and III, was employed to terminate the training process based on different loss thresholds for the two methods. For Method II, training was halted when the loss reached a threshold of 1.28×10^{-4} after nearly 30000 epochs, as further reduction did not consistently improve the performance of test set. For Method III, a threshold of 5.97×10^{-4} was applied, leading to termination after approximately 145000 epochs.

Unlike Method I, both Method II and III utilized a static learning rate of 0.001, achieving satisfactory test performance efficiently while conserving computational resources. The comparison of the three methods is presented in Tab. II.

After training, Method II demonstrated superior accuracy, with RMSD and MAE values of 0.087 MeV and 0.064 MeV for the training set, and 0.143 MeV and 0.099 MeV for the test set. Meanwhile, Method III further enhanced the model's accuracy, achieving RMSD and MAE values of 0.052 MeV and 0.039 MeV for the training set, and 0.122 MeV and 0.087 MeV for the test set. Detailed results for all three methods are presented in Tab. III. Figure 5 visualizes the improved efficiency and accuracy of both Method II (b) and Method III (c) compared to Method I (a) of the prediction errors on the AME2020 dataset and also illustrates the improved accuracy and generalization capability of Method III compared to the other two methods.

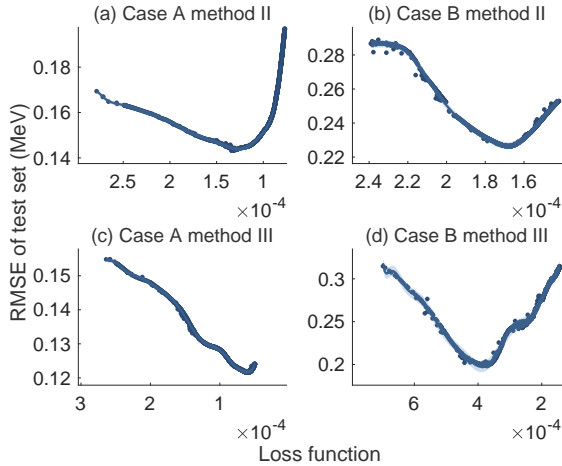


FIG. 4. Variation of the RMSD of test set with the values of the loss function in Case A and B using Method II and III. (a) presents the improved extrapolation within an optimal loss range from 1×10^{-4} to 1.5×10^{-4} , terminating at 1.28×10^{-4} . (b) presents the enhanced extrapolation within 1.6×10^{-4} to 1.8×10^{-4} , terminating at 1.68×10^{-4} . (c) presents the enhanced extrapolation within 0.5×10^{-4} to 0.7×10^{-4} , terminating at 5.97×10^{-5} . (d) presents the enhanced extrapolation within 3×10^{-4} to 5×10^{-4} , terminating at 3.80×10^{-4} . Points represent test set performance for different loss function stopping values, the curve is a polynomial fit, and the shaded area represents fitting error.

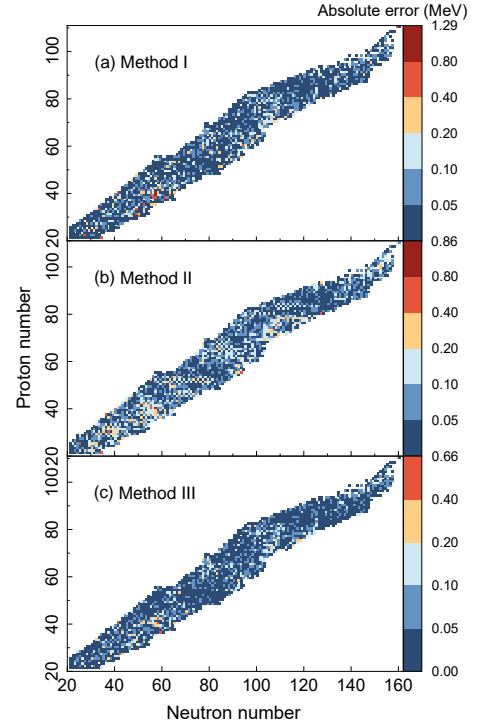


FIG. 5. Prediction errors of three Methods on the AME2020 dataset, with the majority of nuclei exhibiting errors below 100 keV.

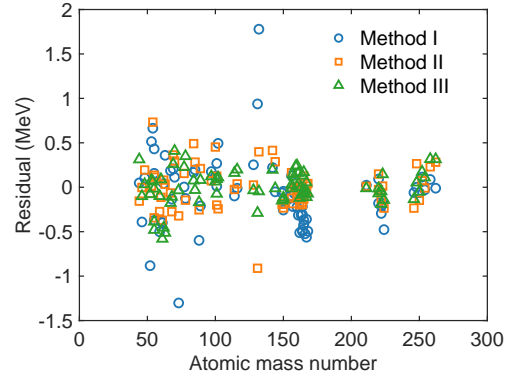


FIG. 6. Comparison of the residual in three Methods in newly added data from AME2020.

B. Case B: prediction of newly added data in AME2020 based on AME2016

In case B, as shown in Fig. 1 (a), we use the entire dataset from AME2016 as the training set, while the data included in AME2020 but not in AME2016 serve as the test set. Training on AME2016 and predicting the data newly added in AME2020 could verify the model's extrapolation capacity. It also provides a basis for a neural network to predict the data not included in AME2020, albeit within a limited extrapolation range. In Method I, an L_2 regularization coefficient of 5×10^{-7} was applied,

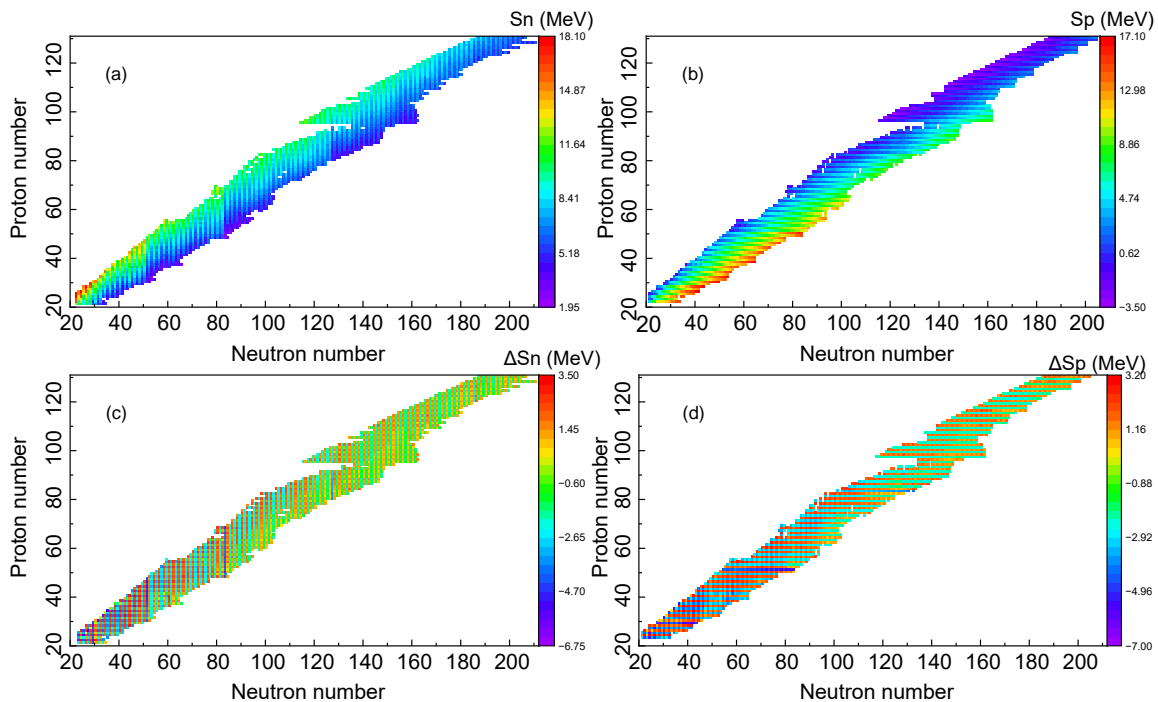


FIG. 7. Predictions of last neutron (S_n) and proton (S_p) separation energy and their rate of changes ΔS_n and ΔS_p .

using the same loss and activation functions as in prior Case A. A dynamic learning rate strategy was employed, with specific learning rate settings detailed in Tab. II. After 3 million epochs, the model achieved an RMSD of 0.195 MeV and an MAE of 0.145 MeV on the training set, while 0.416 MeV and 0.283 MeV on the test set, as shown in Tab. III.

In Method II and III, the network architecture features two hidden layers with 120 neurons and 60 neurons, respectively, which were selected by preliminary experiments. The loss and activation functions remained consistent with previous Case A. Training was terminated via early stopping at a threshold loss value of 1.68×10^{-4} for Method II and 3.80×10^{-4} for Method III, as shown in Fig. 4 (b) and (d).

Unlike Method I, which applied L_2 regularization and a dynamic learning rate, Method II and III used neither, as its larger architecture provided a more stable training process without requiring additional techniques to prevent overfitting. This approach simplified the optimization process by maintaining a constant learning rate throughout. Method II achieved an RMSD of 0.159 MeV and an MAE of 0.122 MeV on the training set, and an RMSD of 0.237 MeV and an MAE of 0.173 MeV on the test set, as shown in Tab. III. Method III achieved an RMSD of 0.125 MeV and an MAE of 0.096 MeV on the training set, while 0.191 MeV and 0.144 MeV on the test set, as shown in Tab. III.

Figure 6 shows the performance comparison of three Methods. It shows that Method II significantly outperforms Method I for most data points, with the RMSD

of Method II reducing values to nearly 40%. Method III significantly outperforms Method II, with the RMSD of Method III reducing values to nearly 20%, highlighting its superior extrapolation capacity.

C. Case C: nucleon pairing correlation, magic number effects, and extrapolations in isotopic chains

To further evaluate Method III, we expand the training data from Case A to examine its ability to capture the physics information embedded in the inputs and reproduce certain physics phenomena. Using AME2020 data, we incorporated theoretical values from the WS4 model as auxiliary inputs to assist in the extrapolation process in the Case C study, as shown in Fig. 1 (b). These values were extended along neutron numbers at fixed proton numbers, focusing on nuclei in regions with experimental errors. In the extrapolated region, corrections accounting for proton and neutron magic number were applied. The training process adhered to the same methodology as Method III in Case A, with the selected learning rate distribution in Tab. II, and the early stopping criterion is adopted. The final RMSD values were 0.106 MeV for the training set and 0.194 MeV for the test set, as shown in Tab. III. The increase is attributed to the relatively large theoretical errors of the newly added samples, ranging from 50 keV and 400 keV. Despite these errors, including these samples remains essential to determine whether the model can learn and reproduce the missing experimental magic number.

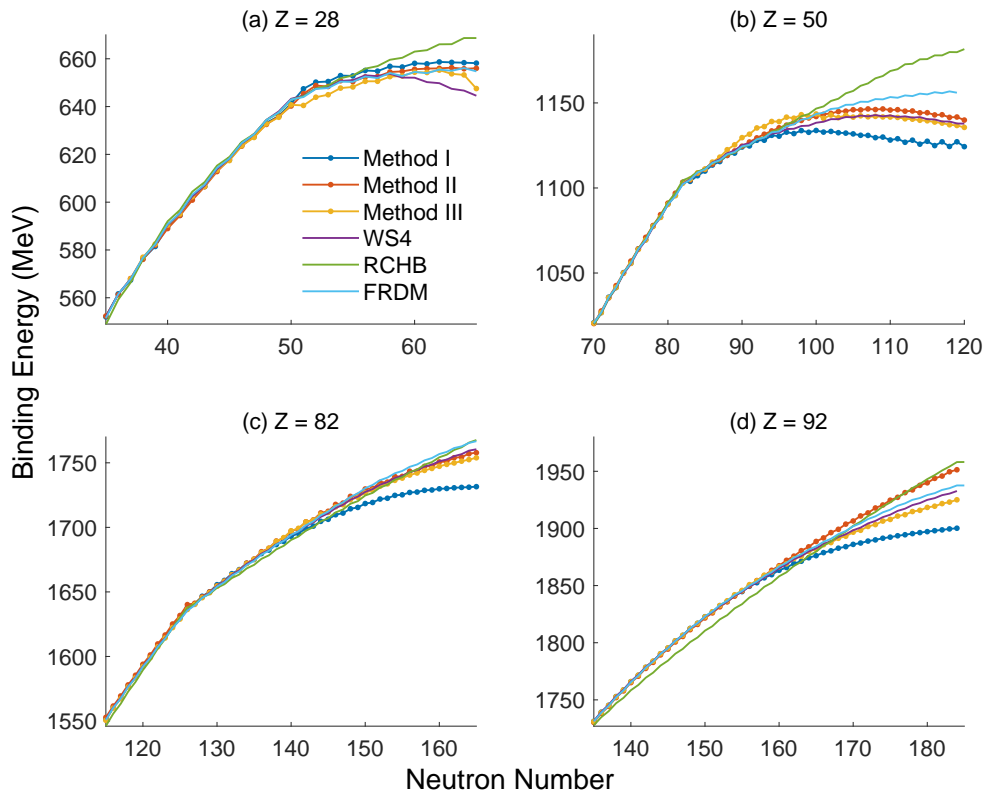


FIG. 8. Comparison of extrapolation in different mass models for (a) $Z = 28$, (b) $Z = 50$, (c) $Z = 82$, and (d) $Z = 92$ isotopes in Method I, II, and III. Lines denote WS4 [24], RCHB [28], and FRDM2012 [21] mass models for comparisons.

The last neutron (S_n) and proton (S_p) separation energy were calculated based on the predicted nuclear masses from FCNN which was configured with 60 neurons in the first hidden layer and 30 neurons in the second hidden layer. The results reveal significant oscillations in S_n and S_p , reflecting the parity of neutron and proton number, indicative of pairing effects in atomic nuclei, as shown in Fig. 7 (a) and (b). To highlight the impact on magic number more clearly, we also calculate their rates of change, presented in Fig. 7 (c) and (d). Abrupt changes near the magic number indicate the enhanced stability of magic nuclei. Figure 7 overall shows that the predicted S_n and S_p , along with their rate changes ΔS_n and ΔS_p , exhibit pronounced variations align with the classical neutron magic number (2, 8, 20, 28, 50, 82, 126) and proton magic number (2, 8, 20, 28, 50, 82). Furthermore, similar behaviors are observed near newly proposed neutron magic number (184, 198) and proton magic numbers (114, 120, 126).

In Case A, we trained and optimized two models that exhibited strong performance within well-studied regions of the nuclear chart. However, while machine learning methods often outperform traditional theoretical approaches within the training datasets, their predictive accuracy tends to diminish significantly in extrapolated regions. To assess the two methods incorporating physics inputs, we evaluated their extrapolation abilities beyond the training set in a statistically robust and physically

meaningful manner, as well as their capability to capture deeper physics principles. We selected four isotopic chains, spanning regions with experimental data to those without. Using two methods, we predicted the binding energies of these isotopes and compared the results with other theoretical approaches. The predictions for four isotopic chains with $Z = 28, 50, 82,$ and 92 , as obtained by Method I, Method II, Method III, WS4, RCHB, and FRDM2012, are shown in Fig. 8.

For the $Z = 28$ isotopic chain, when extrapolated to $N = 55$, the predictions from all methods show negligible differences. However, for $N > 55$, the predictions of Method I, II, III, and FRDM2012 align closely. For the $Z = 50$ isotopic chain, when extrapolated to $N = 95$, the methods again show minimal differences. When $90 < N < 95$, Method III shows slight deviations from the predictions of the other models. For $95 < N < 100$, the predictions from Method II and WS4 remain closely aligned. Beyond $N=100$, the predictions from Method III and WS4 remain closely aligned, whereas Method I begins to diverge significantly from the other models. Although the deviation is less pronounced than that of RCHB. For the $Z = 82$ isotopic chain, when extrapolated to $N = 145$, the results from all methods are similarly consistent. Beyond $N = 145$, Method I's predictions diverge noticeably from those of all other models, while Method II and III maintain the same trend as the other theoretical models. Notably, Method III's predictions ex-

hibit excellent agreement with those of WS4. For the $Z = 92$ isotopic chain, when extrapolated to $N = 160$, all models except RCHB produce predictions with minor differences. However, for $N > 160$, Method I’s predictions deviate from all other methods, while Method III’s predictions align closely with those of RCHB and maintain a smaller gap compared to the other approaches, especially relative to Method I. For the above four isotopic chains, the experimental data used for training are only provided up to $N = [45, 85, 133, 148]$ respectively. While lacking experimental data, the three machine learning methods are still able to align with certain theoretical predictions, demonstrating the extrapolation capability of the physics-informed neural networks.

These results highlight that three distinct Methods demonstrate extrapolation capabilities that are comparable to theoretical models within a certain range. However, the extrapolation capability of Method II and III is notably superior to that of Method I in larger neutron regions. In $Z = 92$, Method III performs better than the other two models, while it’s close to the results predicted by Method II in other Z regions. Over the range of neutron numbers considered in this study, the performance of Method II matches that of the mainstream theoretical models. To the extent that, if the curve labels were removed, it would be challenging to distinguish the machine learning predictions from those of the theoretical models. Our research further illustrates that the physics-informed and rigorously validated FCNN model has the potential to pass a Turing Test in the domain of nuclear mass predictions, demonstrating its utility as a robust tool in this field.

IV. SUMMARY AND OUTLOOK

In summary, this study highlights the potential of FCNNs in atomic mass predictions by combining machine learning techniques with domain-specific physics insights. Three distinct methods were developed: Method I focused on leveraging physics principles as input features to directly represent binding energies. Method II employed a macroscopic-microscopic framework with multi-output training to address complex components like deformation and microscopic corrections. Method III is an extension of Method II with additional refinements, including deformation effects modeled through parameter

adjustments, to further enhance the predictive accuracy. Method III demonstrated superior predictive accuracy, and extrapolation capabilities, as well as the ability to reproduce key physics phenomena such as nucleon pairing effect and magic number. Sensitivity and ablation analyses confirmed the physics interpretability of specific input features, even those with minimal statistical impact. By incorporating predictions from the WS4 model, Method III validated new magic number and provided insights into superheavy nuclei. This work also further compared the mass predictions of all the methods for isotopic chains in regions with sparse experimental data against other theoretical approaches. This study offers a unified framework to advance understanding of nuclear masses and their role in the nuclear landscape.

In the future, machine learning could pave the way for more sophisticated hybrid approaches integrating with nuclear models and experimental analysis. We can extend the studies to encompass diverse nuclear phenomena, improve extrapolation accuracy with innovative network architectures, and explore its broader applications combining with Bayesian emulators [76–79], including hypernuclei properties [80], nuclear structure and initial conditions of quark-gluon plasma (QGP) in relativistic heavy-ion collisions [81–90]. By bridging machine learning and traditional physics-driven approaches, we expect such explorations would propel the physics capabilities of understanding the properties of QGP in theoretical frameworks and experimental techniques at the Relativistic Heavy-Ion Collider (RHIC) and the Large Hadron Collider (LHC) [49, 50].

ACKNOWLEDGMENTS

We would like to thank Wanbing He and Simin Wang for the insightful discussions. This work is supported in part by the National Key Research and Development Program of China under Contract No. 2022YFA1604900, 2024YFA1612600, the National Natural Science Foundation of China (NSFC) under Contract Nos. 12205051, 12025501, 12147101, the Natural Science Foundation of Shanghai under Contract No. 23JC1400200, the STCSM under Grant No. 23590780100, Shanghai Pujiang Talents Program under Contract No. 24PJA009, China Postdoctoral Science Foundation under Grant No. 2024M750489, DOE Research Grant Number DE-SC0024602.

[1] D. Lunney, J. M. Pearson, and C. Thibault, “Recent trends in the determination of nuclear masses,” *Rev. Mod. Phys.* **75**, 1021–1082 (2003).
 [2] Dirk Martin, Almudena Arcones, Witold Nazarewicz, and Erik Olsen, “Impact of nuclear mass uncertainties on the r -process,” *Phys. Rev. Lett.* **116**, 121101 (2016).
 [3] Evgeny Epelbaum, Hans-Werner Hammer, and Ulf-G. Meissner, “Modern Theory of Nuclear Forces,” *Rev.*

Mod. Phys. **81**, 1773–1825 (2009).
 [4] A. Akmal, V. R. Pandharipande, and D. G. Ravenhall, “The Equation of state of nucleon matter and neutron star structure,” *Phys. Rev. C* **58**, 1804–1828 (1998), arXiv:nucl-th/9804027.
 [5] M. Onsi and J. M. Pearson, “Equation of state of stellar nuclear matter and the effective nucleon mass,” *Phys. Rev. C* **65**, 047302 (2002).

- [6] William D. Myers and Wladyslaw J. Swiatecki, “Nuclear masses and deformations,” *Nucl. Phys.* **81**, 1–60 (1966).
- [7] Margaret E. Burbidge, G. R. Burbidge, William A. Fowler, and F. Hoyle, “Synthesis of the elements in stars,” *Rev. Mod. Phys.* **29**, 547–650 (1957).
- [8] M. R. Mumpower, R. Surman, G. C. McLaughlin, and A. Aprahamian, “The impact of individual nuclear properties on r -process nucleosynthesis,” *Prog. Part. Nucl. Phys.* **86**, 86–126 (2016), [Erratum: *Prog. Part. Nucl. Phys.* **87**, 116–116 (2016)].
- [9] H. Schatz *et al.*, “ rp -process nucleosynthesis at extreme temperature and density conditions,” *Phys. Rep.* **294**, 167–263 (1998).
- [10] D. S. Ahn *et al.*, “Location of the Neutron Dripline at Fluorine and Neon,” *Phys. Rev. Lett.* **123**, 212501 (2019).
- [11] Jochen Erler, Noah Birge, Markus Kortelainen, Witold Nazarewicz, Erik Olsen, Alexander M. Perhac, and Mario Stoitsov, “The limits of the nuclear landscape,” *Nature* **486**, 509–512 (2012).
- [12] Georges Audi, “The History of nuclidic masses and of their evaluation,” *Int. J. Mass Spectr. Ion Process.* **251**, 85–94 (2006).
- [13] A. H. Wapstra, G. Audi, and C. Thibault, “The Ame 2003 atomic mass evaluation,” *Nucl. Phys. A* **729**, 129–336 (2003).
- [14] G. Audi, A. H. Wapstra, and C. Thibault, “The Ame2003 atomic mass evaluation (II). Tables, graphs and references,” *Nucl. Phys. A* **729**, 337–676 (2002).
- [15] Wapstra A.H. et al. Audi G., Wang M., “The Ame2012 atomic mass evaluation,” *Chin. Phys. C* **36**, 1287 (2012).
- [16] M. Wang, G. Audi, A. H. Wapstra, F. G. Kondev, M. MacCormick, X. Xu, and B. Pfeiffer, “The Ame2012 atomic mass evaluation,” *Chin. Phys. C* **36**, 1603–2014 (2012).
- [17] W.J. Huang, G. Audi, M. Wang, and et al., “The AME2016 atomic mass evaluation (I). Evaluation of input data; and adjustment procedures,” *Chin. Phys. C* **41**, 030002 (2017).
- [18] H. A. Bethe and R. F. Bacher, “Nuclear Physics A. Stationary States of Nuclei,” *Rev. Mod. Phys.* **8**, 82–229 (1936).
- [19] C. F. V. Weizsacker, “Zur Theorie der Kernmassen,” *Z. Phys.* **96**, 431–458 (1935).
- [20] Z. M. Niu and H. Z. Liang, “Nuclear mass predictions with machine learning reaching the accuracy required by r -process studies,” *Phys. Rev. C* **106**, L021303 (2022).
- [21] P. Möller, A. J. Sierk, T. Ichikawa, and H. Sagawa, “Nuclear ground-state masses and deformations: FRDM(2012),” *Atom. Data Nucl. Data Tabl.* **109-110**, 1–204 (2016).
- [22] Y. Aboussir, J. M. Pearson, A. K. Dutta, and F. Tondeur, “Nuclear mass formula via an approximation to the Hartree–Fock method,” *Atom. Data Nucl. Data Tabl.* **61**, 127–176 (1995).
- [23] S. Goriely, N. Chamel, and J. M. Pearson, “Further explorations of Skyrme–Hartree–Fock–Bogoliubov mass formulas. 13. The 2012 atomic mass evaluation and the symmetry coefficient,” *Phys. Rev. C* **88**, 024308 (2013).
- [24] Ning Wang, Min Liu, Xizhen Wu, and Jie Meng, “Surface diffuseness correction in global mass formula,” *Phys. Lett. B* **734**, 215–219 (2014).
- [25] P. Ring, “Relativistic mean field in finite nuclei,” *Prog. Part. Nucl. Phys.* **37**, 193–263 (1996).
- [26] D. Vretenar, A. V. Afanasjev, G. A. Lalazissis, and P. Ring, “Relativistic Hartree Bogoliubov theory: static and dynamic aspects of exotic nuclear structure,” *Phys. Rep.* **409**, 101–259 (2005).
- [27] Shan-Gui Zhou, “Multidimensionally constrained covariant density functional theories—nuclear shapes and potential energy surfaces,” *Phys. Scripta* **91**, 063008 (2016).
- [28] X. W. Xia *et al.*, “The limits of the nuclear landscape explored by the relativistic continuum Hartree–Bogoliubov theory,” *Atom. Data Nucl. Data Tabl.* **121-122**, 1–215 (2018).
- [29] P. W. Zhao, Z. P. Li, J. M. Yao, and J. Meng, “New parametrization for the nuclear covariant energy density functional with point-coupling interaction,” *Phys. Rev. C* **82**, 054319 (2010).
- [30] Kaiyuan Zhang *et al.* (DRHBc Mass Table), “Nuclear mass table in deformed relativistic Hartree–Bogoliubov theory in continuum, I: Even–even nuclei,” *Atom. Data Nucl. Data Tabl.* **144**, 101488 (2022).
- [31] Peng Guo *et al.* (DRHBc Mass Table), “Nuclear mass table in deformed relativistic Hartree–Bogoliubov theory in continuum, II: Even-Z nuclei,” *Atom. Data Nucl. Data Tabl.* **158**, 101661 (2024).
- [32] Raditya Utama and Jorge Piekarewicz, “Refining mass formulas for astrophysical applications: a Bayesian neural network approach,” *Phys. Rev. C* **96**, 044308 (2017).
- [33] Tian Shuai Shang, Hui Hui Xie, Jian Li, and Haozhao Liang, “Global prediction of nuclear charge density distributions using a deep neural network,” *Phys. Rev. C* **110**, 014308 (2024).
- [34] Yanhua Lu, Tianshuai Shang, Pengxiang Du, Jian Li, Haozhao Liang, and Zhongming Niu, “Nuclear mass predictions based on convolutional neural network,” arXiv:2404.14948 [nucl-th].
- [35] R. Utama and J. Piekarewicz, “Validating neural-network refinements of nuclear mass models,” *Phys. Rev. C* **97**, 014306 (2018).
- [36] Chen-Qi Li, Chao-Nan Tong, Hong-Jing Du, and Long-Gang Pang, “Deep learning approach to nuclear masses and α -decay half-lives,” *Phys. Rev. C* **105**, 064306 (2022).
- [37] Lin-Xing Zeng, Yu-Ying Yin, Xiao-Xu Dong, and Li-Sheng Geng, “Nuclear binding energies in artificial neural networks,” *Phys. Rev. C* **109**, 034318 (2024).
- [38] Yunfei Ma, Chen Su, Jian Liu, Zhongzhou Ren, Chang Xu, and Yonghao Gao, “Predictions of nuclear charge radii and physical interpretations based on the naive Bayesian probability classifier,” *Phys. Rev. C* **101**, 014304 (2020).
- [39] Xiao-Xu Dong, Rong An, Jun-Xu Lu, and Li-Sheng Geng, “Novel Bayesian neural network based approach for nuclear charge radii,” *Phys. Rev. C* **105**, 014308 (2022).
- [40] Z. M. Niu, H. Z. Liang, B. H. Sun, W. H. Long, and Y. F. Niu, “Predictions of nuclear β -decay half-lives with machine learning and their impact on r -process nucleosynthesis,” *Phys. Rev. C* **99**, 064307 (2019).
- [41] Zisheng Jin, Mingshuai Yan, Hao Zhou, An Cheng, Zhongzhou Ren, and Jian Liu, “Bayesian optimization approach to model-based description of α decay,” *Phys. Rev. C* **108**, 014326 (2023).
- [42] Na-Na Ma, Tian-Liang Zhao, Wen-Xia Wang, and Hong-Fei Zhang, “Simple deep-learning approach for α -decay half-life studies,” *Phys. Rev. C* **107**, 014310 (2023).

- [43] Hiroki Iwamoto, Shin-ichiro Meigo, and Kenta Sugihara, “Comprehensive estimation of nuclide production cross sections using a phenomenological approach,” *Phys. Rev. C* **109**, 054610 (2024).
- [44] Sinjini Mitra, Hongjun Choi, Shusen Liu, Ruben Glatt, Kyle Wendt, and Nicolas Schunck, “Unmasking Correlations in Nuclear Cross Sections with Graph Neural Networks,” arXiv:2404.02332 [nucl-th].
- [45] Yuan Lin, Jia-Xing Li, and Hong-Fei Zhang, “Transfer learning and neural networks in predicting quadrupole deformation,” *Chin. Phys. C* **48**, 064106 (2024).
- [46] B. F. Lv, Z. L. Li, Y. J. Wang, and C. M. Petrache, “Mapping low-lying states and $B(E2;01+\rightarrow 21+)$ in even-even nuclei with machine learning,” *Phys. Lett. B* **857**, 139013 (2024).
- [47] Zu-Xing Yang, Xiao-Hua Fan, Zhi-Pan Li, and Shunji Nishimura, “A neural network approach for orienting heavy-ion collision events,” *Phys. Lett. B* **848**, 138359 (2024).
- [48] Yu-Gang Ma, Long-Gang Pang, Rui Wang, and Kai Zhou, “Phase Transition Study Meets Machine Learning,” *Chin. Phys. Lett.* **40**, 122101 (2023).
- [49] Wan-Bing He, Yu-Gang Ma, Long-Gang Pang, Hui-Chao Song, and Kai Zhou, “High-energy nuclear physics meets machine learning,” *Nucl. Sci. Tech.* **34**, 88 (2023).
- [50] Kai Zhou, Lingxiao Wang, Long-Gang Pang, and Shuzhe Shi, “Exploring QCD matter in extreme conditions with Machine Learning,” *Prog. Part. Nucl. Phys.* **135**, 104084 (2024).
- [51] Shuang Guo, Han-Sheng Wang, Kai Zhou, and Guo-Liang Ma, “Machine learning study to identify collective flow in small and large colliding systems,” *Phys. Rev. C* **110**, 024910 (2024).
- [52] Rui Wang, Yu-Gang Ma, R. Wada, Lie-Wen Chen, Wan-Bing He, Huan-Ling Liu, and Kai-Jia Sun, “Nuclear liquid-gas phase transition with machine learning,” *Phys. Rev. Res.* **2**, 043202 (2020).
- [53] Yi-Dan Song, Rui Wang, Yu-Gang Ma, Xian-Gai Deng, and Huan-Ling Liu, “Determining the temperature in heavy-ion collisions with multiplicity distribution,” *Phys. Lett. B* **814**, 136084 (2021), arXiv:2101.10613 [nucl-th].
- [54] Jinhui Chen *et al.*, “Properties of the QCD matter: review of selected results from the relativistic heavy ion collider beam energy scan (RHIC BES) program,” *Nucl. Sci. Tech.* **35**, 214 (2024).
- [55] Qi-Ye Shou *et al.*, “Properties of QCD matter: a review of selected results from ALICE experiment,” *Nucl. Sci. Tech.* **35**, 219 (2024).
- [56] Zepeng Gao and Qinggeng Li, “Studies on several problems in nuclear physics by using machine learning,” *Nucl. Tech.* **46**, 080009 (2023).
- [57] Wanbing He, Qingfeng Li, Yugang Ma, Zhongming Niu, Junchen Pei, and Yingxun Zhang, “Machine learning in nuclear physics at low and intermediate energies,” *Sci. China Phys. Mech. Astron.* **66**, 282001 (2023).
- [58] Esra Yüksel, Derya Soydaner, and Hüseyin Bahtiyar, “Nuclear binding energy predictions using neural networks: Application of the multilayer perceptron,” *Int. J. Mod. Phys. E* **30**, 2150017 (2021).
- [59] Zepeng Gao, Yongjia Wang, Hongliang Lü, Qingfeng Li, Caiwan Shen, and Ling Liu, “Correction to: Machine learning the nuclear mass,” *Nucl. Sci. Tech.* **32**, 118 (2021).
- [60] Esra Yüksel, Derya Soydaner, and Hüseyin Bahtiyar, “Nuclear mass predictions using machine learning models,” *Phys. Rev. C* **109**, 064322 (2024).
- [61] Léo Neufcourt, Yuchen Cao, Witold Nazarewicz, and Frederi Viens, “Bayesian approach to model-based extrapolation of nuclear observables,” *Phys. Rev. C* **98**, 034318 (2018).
- [62] Michael Kohler and Sophie Langer, “On the rate of convergence of fully connected deep neural network regression estimates,” *Ann. Stat.* **49**, 2231 – 2249 (2021).
- [63] Kurt Hornik, Maxwell Stinchcombe, and Halbert White, “Multilayer feedforward networks are universal approximators,” *Neural Networks* **2**, 359–366 (1989).
- [64] Meng Wang, W. J. Huang, F. G. Kondev, G. Audi, and S. Naimi, “The AME 2020 atomic mass evaluation (II). Tables, graphs and references,” *Chin. Phys. C* **45**, 030003 (2021).
- [65] Meng Wang, G. Audi, F. G. Kondev, W. J. Huang, S. Naimi, and Xing Xu, “The AME2016 atomic mass evaluation (II). Tables, graphs and references,” *Chin. Phys. C* **41**, 030003 (2017).
- [66] Ning Wang, Zuoying Liang, Min Liu, and Xizhen Wu, “Mirror nuclei constraint in mass formula,” *Phys. Rev. C* **82**, 044304 (2010).
- [67] J. Duflo and A. P. Zuker, “Microscopic mass formulae,” *Phys. Rev. C* **52**, R23 (1995), arXiv:nucl-th/9505011.
- [68] O. Sorlin and M. G. Porquet, “Nuclear magic numbers: New features far from stability,” *Prog. Part. Nucl. Phys.* **61**, 602–673 (2008), arXiv:0805.2561 [nucl-ex].
- [69] Michael Bender, Paul-Henri Heenen, and Paul-Gerhard Reinhard, “Self-consistent mean-field models for nuclear structure,” *Rev. Mod. Phys.* **75**, 121–180 (2003).
- [70] J. Meng, H. Toki, S. G. Zhou, S. Q. Zhang, W. H. Long, and L. S. Geng, “Relativistic Continuum Hartree Bogoliubov theory for ground state properties of exotic nuclei,” *Prog. Part. Nucl. Phys.* **57**, 470–563 (2006), arXiv:nucl-th/0508020.
- [71] Walter Greiner, Joachim A Maruhn, *et al.*, *Nuclear models*, Vol. 261 (Springer, 1996).
- [72] Hwanjun Song, Minseok Kim, Dongmin Park, Yooju Shin, and Jae-Gil Lee, “Learning from noisy labels with deep neural networks: A survey,” *IEEE T. Neur. Net. Lear.* **34**, 8135–8153 (2022).
- [73] Junteng Jia and Austion R Benson, “Residual correlation in graph neural network regression,” in *Proceedings of the 26th ACM SIGKDD international conference on knowledge discovery & data mining* (2020) pp. 588–598.
- [74] Dan Hendrycks and Kevin Gimpel, “Gaussian error linear units (gelus),” arXiv:1606.08415 (2016).
- [75] Minhyeok Lee, “Gelu activation function in deep learning: a comprehensive mathematical analysis and performance,” arXiv:2305.12073 (2023).
- [76] Wenjie Xie, Ma Ziwei, and Guo Junhua, “Bayesian inference of the crust-core transition density via the neutron-star radius and neutron-skin thickness data,” *Nucl. Sci. Tech.* **34**, 91 (2023).
- [77] Jia Zhou and Jun Xu, “Bayesian inference of neutron-skin thickness and neutron-star observables based on effective nuclear interactions,” *Sci. China Phys. Mech. Astron.* **67**, 282011 (2024).
- [78] E. Alhassan, D. Rochman, G. Schnabel, and A. J. Koning, “Bayesian model averaging (BMA) for nuclear data evaluation,” *Nucl. Sci. Tech.* **35**, 205 (2024).
- [79] Mubarak Alqahtani, Rajeev S. Bhalariao, Giuliano Giacalone, Andreas Kirchner, and Jean-Yves Ollitrault,

- “Impact parameter dependence of anisotropic flow: Bayesian reconstruction in ultracentral nucleus-nucleus collisions,” *Phys. Rev. C* **110**, 064906 (2024).
- [80] J. Adam *et al.* (STAR), “Measurement of the mass difference and the binding energy of the hypertriton and antihypertriton,” *Nature Phys.* **16**, 409–412 (2020).
- [81] M. I. Abdulhamid *et al.* (STAR), “Imaging shapes of atomic nuclei in high-energy nuclear collisions,” *Nature* **635**, 67–72 (2024).
- [82] Jianguong Jia *et al.*, “Imaging the initial condition of heavy-ion collisions and nuclear structure across the nuclide chart,” *Nucl. Sci. Tech.* **35**, 220 (2024).
- [83] Chunjian Zhang and Jianguong Jia, “Evidence of Quadrupole and Octupole Deformations in $Zr^{96}+Zr^{96}$ and $Ru^{96}+Ru^{96}$ Collisions at Ultrarelativistic Energies,” *Phys. Rev. Lett.* **128**, 022301 (2022).
- [84] Giuliano Giacalone, Jianguong Jia, and Chunjian Zhang, “Impact of Nuclear Deformation on Relativistic Heavy-Ion Collisions: Assessing Consistency in Nuclear Physics across Energy Scales,” *Phys. Rev. Lett.* **127**, 242301 (2021).
- [85] Long-Gang Pang, Kai Zhou, and Xin-Nian Wang, “Interpretable deep learning for nuclear deformation in heavy ion collisions,” arXiv:1906.06429 [nucl-th].
- [86] Yilong Yang and Pengwei Zhao, “Deep-neural-network approach to solving the ab initio nuclear structure problem,” *Phys. Rev. C* **107**, 034320 (2023).
- [87] Giacalone Giuliano, “Beyond axial symmetry: high-energy collisions unveil the ground-state shape of ^{238}U ,” *Nucl. Sci. Tech.* **35**, 218 (2024).
- [88] Hengfeng Huang, Bowen Xiao, Ziming Liu, Zeming Wu, Yadong Mu, and Huichao Song, “Applications of deep learning to relativistic hydrodynamics,” *Phys. Rev. Res.* **3**, 023256 (2021).
- [89] Long-Gang Pang, Kai Zhou, Nan Su, Hannah Petersen, Horst Stöcker, and Xin-Nian Wang, “An equation-of-state-meter of quantum chromodynamics transition from deep learning,” *Nature Commun.* **9**, 210 (2018).
- [90] Fu-Peng Li, Hong-Liang Lü, Long-Gang Pang, and Guang-You Qin, “Deep-learning quasi-particle masses from QCD equation of state,” *Phys. Lett. B* **844**, 138088 (2023).